The Astronomical Journal, 129:2268–2280, 2005 May

HUBBLE SPACE TELESCOPE IMAGING OF THE PRIMARY SHOCK FRONT IN THE CYGNUS LOOP SUPERNOVA REMNANT[1]

William P. Blair and Ravi Sankrit
Department of Physics and Astronomy, Johns Hopkins University, 3400 North Charles Street, Baltimore, MD 21218; wpb@pha.jhu.edu, ravi@pha.jhu.edu

and

John C. Raymond
Harvard-Smithsonian Center for Astrophysics, 60 Garden Street, Cambridge, MA 02138; raymond@cfa.harvard.edu
Received 2004 December 6; accepted 2005 January 22

ABSTRACT

We present *Hubble Space Telescope* WFPC2 narrowband Hα (F656N) and [O III] λ5007 (F502N) imaging of two fields on the northeastern limb of the Cygnus Loop supernova remnant. This region provides an outstanding example of the initial encounter between the primary blast wave and the surrounding interstellar medium. The Hα images show the primary nonradiative shock front, which, when viewed edge-on, is unresolved at WFPC2 resolution. The [O III] images show portions of filaments that are beginning to become radiative, and in these images the filaments are resolved, appearing fuzzy at WFPC2 resolution. The [O III] filament regions are not bounded directly by Hα filaments, indicating that the shock emission from the nascent radiative region is sufficient to fully ionize the local preshock gas. One field, imaged 4 yr earlier in Hα with WFPC2, is used to study the proper motion of the filament and constrain any brightness variations over this time period. In conjunction with improved models of nonradiative shocks, these data are used to place limits on the possible deceleration of the filament and refine the distance to the Cygnus Loop, arriving at a revised value of $d = 540^{+100}_{-80}$ pc (assuming no deceleration). The second field imaged contains examples of coherent Hα filaments with much more dramatic curvatures than identified previously. We discuss the possible reasons for the different morphology of these filaments and conclude that they can be accommodated with relatively modest variations in local density and shock velocity.

Key words: ISM: individual (Cygnus Loop) — shock waves — supernova remnants

Online material: color figure

1. INTRODUCTION

The Cygnus Loop supernova remnant (SNR) is an extremely important object of study, often being called the prototypical middle-aged SNR. Its proximity, large angular size, and relatively small foreground extinction all help make it an important object for studies across the electromagnetic spectrum. The current picture of the Cygnus Loop is one of a cavity explosion of a fairly massive star (Levenson et al. 1997; Leahy 2002), where the interaction of the blast wave with the walls of the cavity have begun only in the relatively recent past. The structure and kinematics of this cavity have been elucidated further by Leahy (2003, 2004).

In a previous paper (Blair et al. 1999, hereafter Paper I), we reported a study of the northeastern limb of this SNR using a WFPC2 Hα image in comparison to a ground-based image to place new constraints on the distance to the Cygnus Loop. In this paper, we expand on this previous study in two ways, reporting WFPC2 Hα and [O III] λ5007 images of two fields along the northeastern rim of the remnant. One field nearly duplicates the field coverage from Paper I, permitting us to study two epochs of *Hubble Space Telescope* (*HST*) Hα data for the same filaments and thus revisit the distance question. The nonradiative filaments in each field primarily emit Hα, but ground-based data (see Hester et al. 1994, hereafter HRB94) indicated selected filaments in each field were also visible in deep [O III] images. We wanted to study both the relative morphology and spatial positioning of the Hα- and [O III]-emitting filaments to understand the process whereby nonradiative filaments "turn on" (become radiative). The Hα image of the second field also provides an example of nonradiative shock filaments with more significant curvature changes than seen in the previous observations.

2. OBSERVATIONS

The regions in the northeastern Cygnus Loop observed with the WFPC2 camera on *HST* are indicated in Figure 1. Both fields are located on faint outer filaments visible primarily in Hα. These faint filaments are $\sim 5'$ beyond the bright arcs of radiative filament emission normally associated with the eastern Cygnus Loop "Veil Nebula" region (NGC 6992). These faint filaments bound regions of bright soft X-ray emission from the SNR. These nonradiative filaments represent locations where the primary shock front is currently encountering material that is at least partially neutral (Chevalier et al. 1980). The field to the lower left in Figure 1 corresponds to the region observed in Paper I, and is referred to as field 1, while the region farther to the upper right, which has not been observed previously with *HST*, is referred to as field 2.

Fields 1 and 2 were observed with the WFPC2 camera on *HST* as part of a Cycle 10 program (GO-9080), using the F656N filter to isolate Hα λ6563 and the F502N filter to isolate

[1] Based on observations with the NASA/ESA *Hubble Space Telescope*, obtained at the Space Telescope Science Institute (STScI), which is operated by the Association of Universities for Research in Astronomy (AURA), Inc., under NASA contract NAS5-26555.

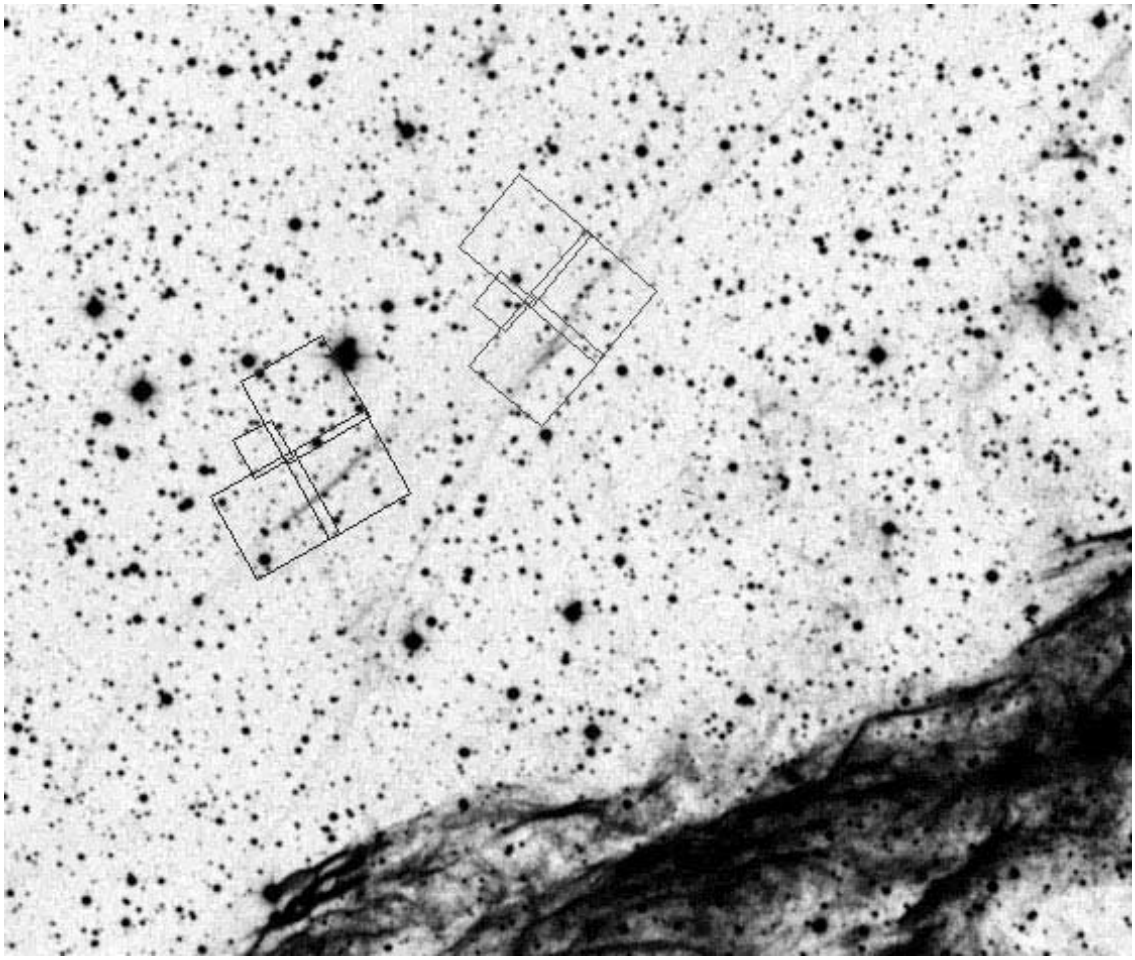

FIG. 1.—Overview of the northeast limb of the Cygnus Loop, showing the locations and orientations of the two WFPC2 fields of view. North is up, and east is to the left. The southeastern field corresponds with the region observed by Blair et al. (1999) and is referred to as field 1. The northwestern field is referred to as field 2.

emission from [O III] λ5007. The nonradiative filaments in each field primarily emit Hα, but ground-based data (cf. HRB94) indicated that selected filaments in each field were visible in deep [O III] images. We thus wanted to study both the relative morphology and spatial positioning of the Hα and [O III] filaments to understand the process whereby nonradiative filaments "turn on" (become radiative). Because the density of stars is low, no separate continuum images were deemed necessary to diagnose stellar confusion. Basic information about the observations is summarized in Table 1, including the earlier (epoch 1) data set on field 1 for reference. Note that although the [O III] and Hα observations of field 1 were taken about a month apart, the same orientation on the sky was used for both. The orientation was about 5° different than for the epoch 1 Hα data on field 1, however.

We have worked directly with the calibrated data extracted from the Guest Observer files provided by the STScI, using tasks available in the IRAF/STSDAS environment.[2] In each field, the primary dimension of the SNR filaments was placed so that it crossed the WF2 and WF3 CCDs. In field 2, faint Hα filaments are also visible crossing the WF4 chip and at very low signal-to-noise ratio across PC1 as well. We used two exposures per orbit to allow removal of cosmic rays, and an offset strategy (as described

[2] IRAF is distributed by the National Optical Astronomy Observatories, which is operated by AURA, Inc., under cooperative agreement with the National Science Foundation. The Space Telescope Science Data Analysis System (STSDAS) is distributed by the STScI.

TABLE 1
OBSERVATION LOG

Parameter	Epoch 1	Epoch 2
Field 1		
R.A. (J2000.0)	$20^h56^m2^s.7$	$20^h56^m2^s.7$
Decl. (J2000.0)	+31°56′39″.1	+31°56′39″.2
Obs. Date (F656N)	1997 Nov 16	2001 Nov 14
t (F656N)	7400 s	7400 s
Obs. Date (F502N)	...	2001 Oct 18
t (F502N)	...	15600 s
Orientation	30°.24	35°.26
Field 2		
R.A. (J2000.0)	...	$20^h55^m48^s.53$
Decl. (J2000.0)	...	+31°59′14″.7
Obs. Date	...	2001 Oct 18
t (F656N)	...	7400 s
t (F502N)	...	15600 s
Orientation	...	50°.26

NOTE.—Coordinates are as specified for the WF-ALL aperture location in the planning files. The WF-ALL location is on the WF3 CCD near the corner that abuts the PC1 CCD.

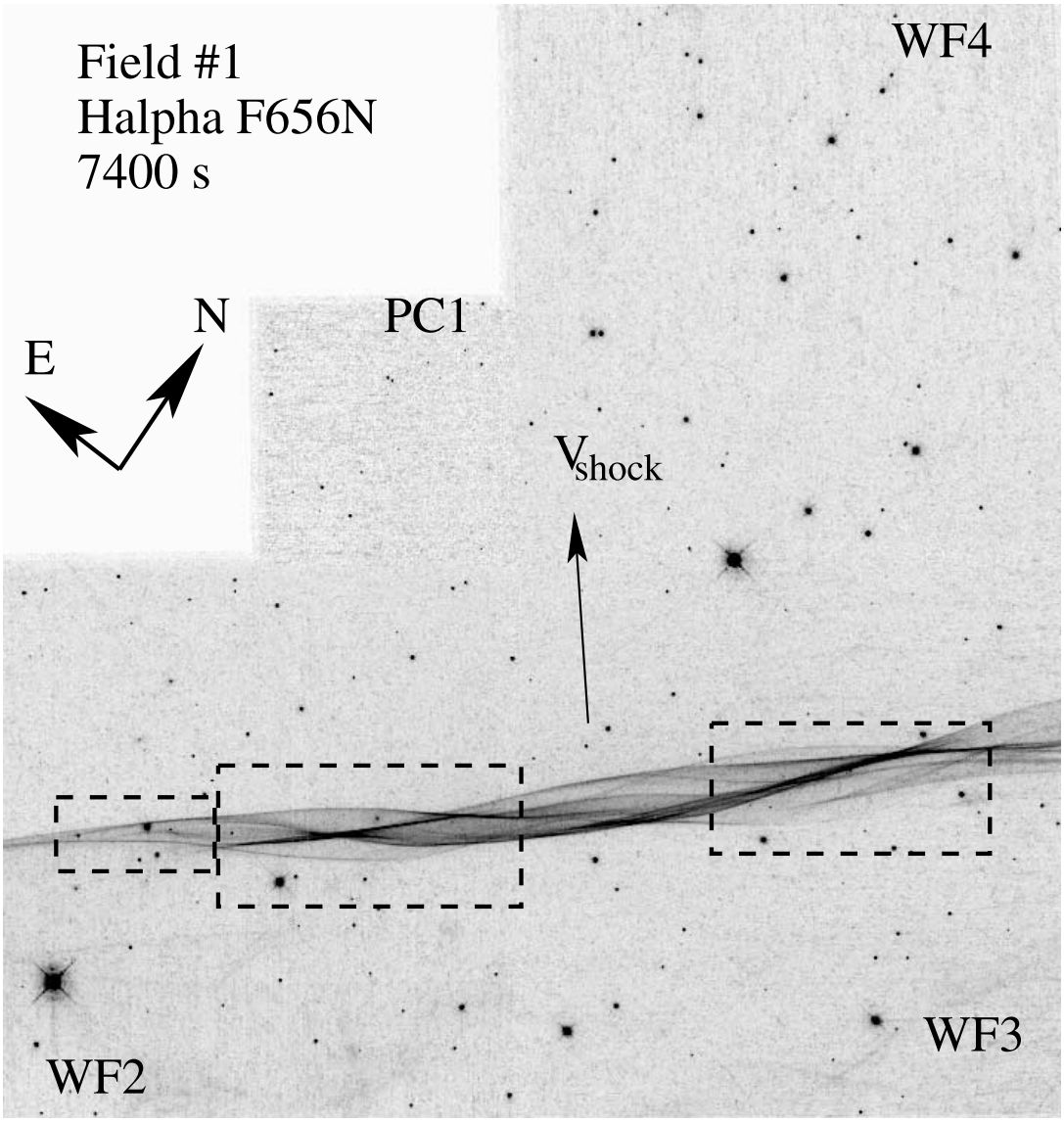

FIG. 2.—Full *HST* WFPC2 field-of-view Hα image of field 1. North is at the upper right, and east is to the upper left as indicated. The gray scaling of this and following figures is linear and set to maximize the appearance of the faint SNR filaments, which in each case are only a few tens of counts per pixel above background in the brightest regions. The shock wave is moving upward in this figure, with the interior of the SNR toward the bottom. Dashed boxes indicate the regions enlarged in Fig. 7.

in Paper I) to also effectively remove hot camera pixels. The positioning was offset by $\Delta x = \Delta y = 10$ WFC pixels ($1''$) between each of three orbits (for the F656N data) and between sets of two orbits for the F502N data. The two exposures from each orbit were combined individually to remove most of the cosmic ray events. Then the data from the first and third shifted positions were aligned with the data from the middle position and combined. The task *wmosaic* was used to produce the full-field images shown in Figures 2 and 3 (field 1) and Figures 4 and 5 (field 2).

The appearance of the Hα filaments in field 1 have been described at length in Paper I. The field 2 filaments are comparable in peak surface brightness and appearance to those in field 1, but the morphology and projection effects are even more complicated than in field 1. The brightest filaments in field 2 are on the WF2 chip, but following them onto the WF3 chip they become fainter and one sees some filaments that arc strongly toward the upper right, connecting with the faint filaments that straddle the WF3-WF4 chip boundary. This strong curvature is very different than is seen in field 1, and is discussed separately below.

Both fields contain some emission in [O III], but even with the long exposures used here this emission is extremely faint. To better show the relative spatial positions of the Hα- and [O III]-emitting regions, we have combined the aligned images in separate colors, as shown in Figure 6. The F656N data are shown in red and the F502N data are shown in green. In field 1, the brightest [O III] emission appears on WF3 and lies somewhat behind (below) the primary Hα filaments. The [O III] emission appears to be the extension of a faint Hα filament (seen to the left) that has faded out. The [O III] emission is considerably more diffuse in appearance than the Hα, and offset downstream (down in the figures) from the Hα. A higher surface brightness embedded knot of [O III] is seen adjacent to a star. Other exceedingly faint [O III] emission is visible in the field (see Fig. 3), including some coincident with the brightest arc of Hα emission and a large area of diffuse emission on the lower half of the WF2 chip. This region is better seen in deep ground-based [O III] images (e.g., HRB94), and the data here simply confirm that it does not resolve into finer structure when viewed at higher spatial resolution.

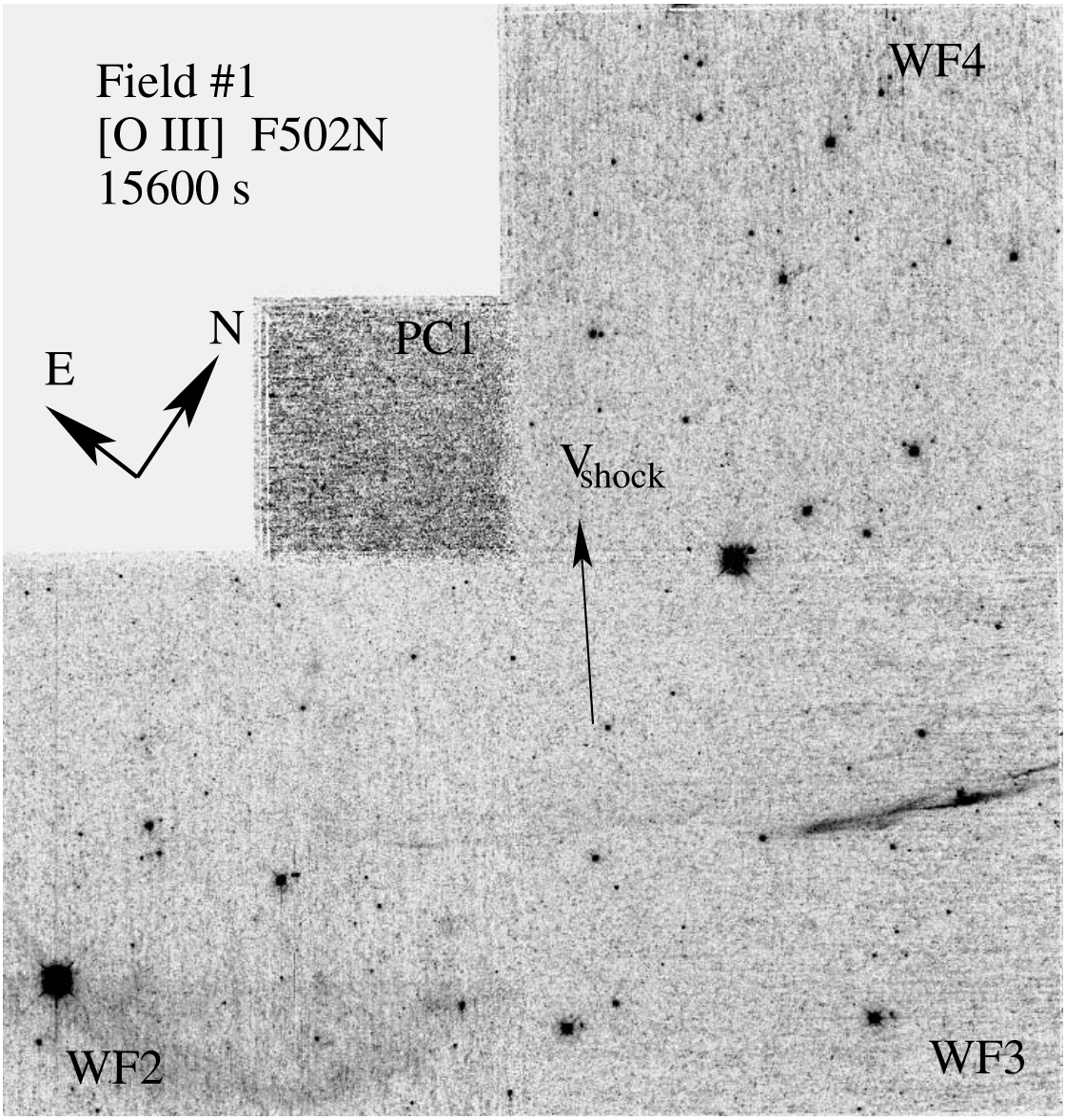

FIG. 3.—Full *HST* WFPC2 field-of-view [O III] image of field 1. Orientation and scale are the same as in Fig. 2.

In field 2, the primary [O III] emission region appears as a diffuse band straddling the WF2-WF3 chip boundary (Fig. 6, *bottom*). Although it is diffuse, this [O III] emission is extensive enough to show some signs of splitting (i.e., separate tangencies) and projection effects as seen in the Hα emission. As with the field 1 filament, the field 2 [O III] filament appears to extend northwestward from a fading Hα filament, although the complicated projection effects in the region make it difficult to discern exactly which Hα filament (or filaments) correspond with the [O III] emission. Other [O III] emission visible in Figure 5 includes faint emission associated with the brightest Hα filament on the WF3 chip and a diffuse patch of [O III] emission with no apparent Hα counterpart on the WF3 chip just below the center of the primary [O III] emission.

3. ANALYSIS

3.1. *The Cygnus Loop Distance Revisited*

Paper I provided a detailed discussion and derivation of the distance to the Cygnus Loop by measuring the proper motion of the field 1 filament from comparison of the WFPC2 image with ground-based data from 1953 and using spectroscopically derived velocity estimates for the shock front at this location. The conclusion was that the distance was considerably lower than the canonical distance estimate of 770 pc attributed to Minkowski (1958); Paper I concluded $d = 440^{+130}_{-100}$ pc. The biggest uncertainties were caused by the error in the proper motion (due to the relatively low resolution of the ground-based data) and uncertainties in assumptions about the equilibration of electrons and ions in the postshock gas, which affected estimates of the shock velocity of the filament. Also, in the context of the cavity model for the Cygnus Loop (Levenson et al. 1997), the possibility existed that the filament might have undergone a significant deceleration over the $\sim$44 yr between the two data sets used to determine the proper motion. This would make a strict combination of the observed proper motion and measured shock velocity inaccurate. The new Hα data for field 1 permits us to address the issue of possible deceleration by determining the proper motion directly from the two epochs of *HST* data. Also, significant new observations (Sankrit et al.

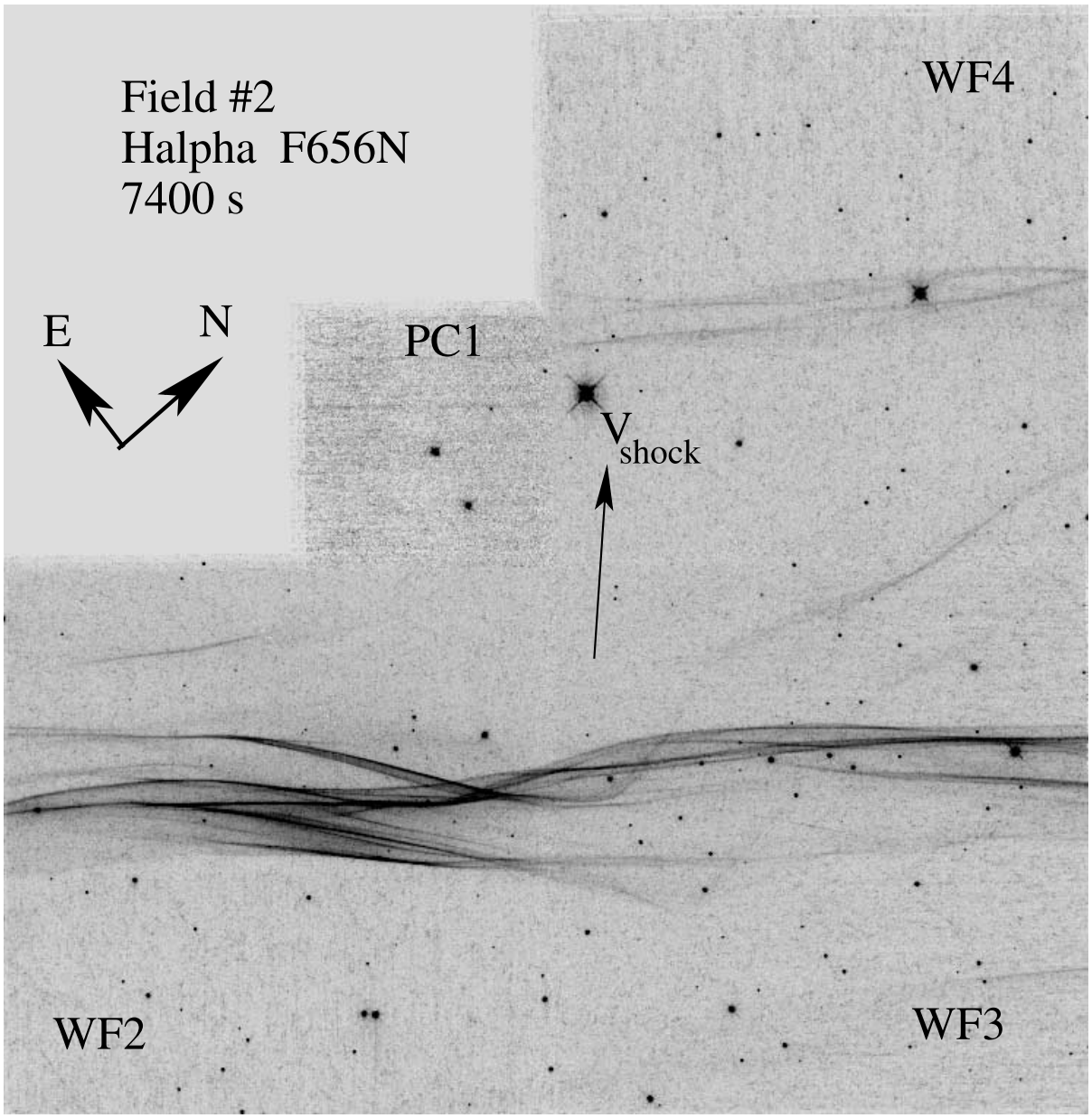

FIG. 4.—Full *HST* WFPC2 field-of-view Hα image of field 2. North is at the upper right, and east is to the upper left, but at a different angle than for field 1. As in the earlier figures, the shock wave is moving upward in this figure, with the interior of the SNR toward the bottom.

2000; Sankrit & Blair 2002) and work on particle equilibration in shocks (Ghavamian et al. 2001) has occurred since Paper I. We discuss these issues below and reexamine the distance to the Cygnus Loop.

3.1.1. *Proper Motion from HST Images*

We have used the two epochs of *HST* Hα imagery of field 1 to study the motion of the filamentary structure in this region. The epoch 1 data were carefully rotated and aligned to the epoch 2 data using 35 stars in the joint field of view. The residuals of measured stellar centroids from this process were random in direction and at a level of 0.3 pixels (0.″03), indicating that none of the stars have abnormally large proper motion that would affect the analysis.

The outward motion of the field 1 filaments is immediately obvious by comparing the data sets. We display these motions in several ways that highlight various aspects of the data. In Figure 7, we present the aligned subimages of some of the sharpest tangencies that show the motion directly. The 2001 image is shown in red and the rotated and aligned 1997 image is shown in green. Regions where emission is bright in both epochs appear yellow, but there are numerous examples where the bulk offset of the red image relative to the green is obvious and resolved. It is clear from this comparison that the filament motion has been very uniform, with no obvious examples of the filament motion being faster or slower in local regions along the tangencies. Furthermore, there are no obvious changes in the relative brightnesses of the filament with spatial position.

In Figure 8, we show a different comparison of the two data sets. In this case, we have created a "difference image" by simply subtracting the aligned 1997 data frame from the 2001 data frame. The small but systematic outward (upward in the figure) motion is obvious across the entire filamentary structure,

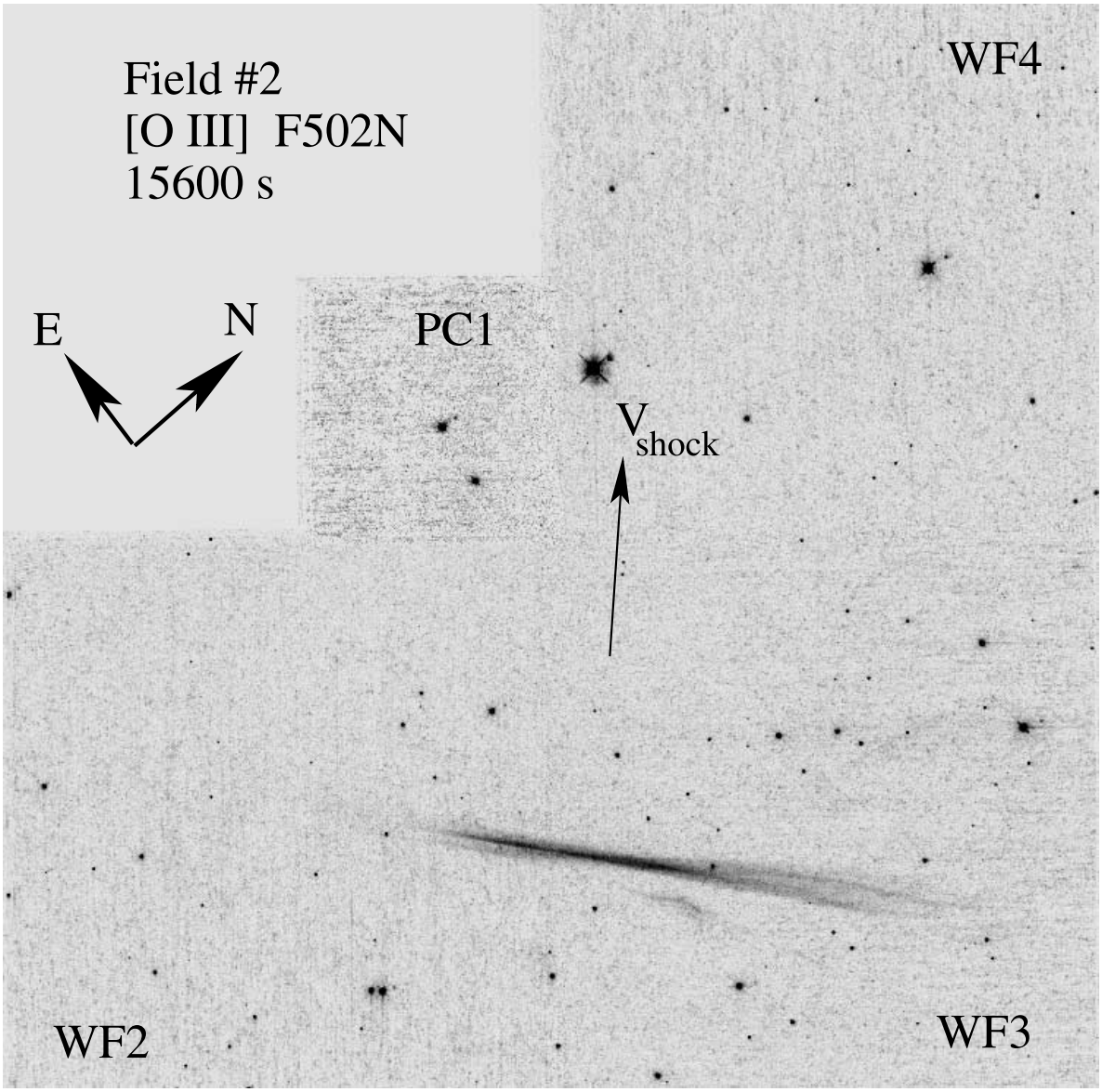

Fig. 5.—Full *HST* WFPC2 field-of-view [O III] image of field 2. Orientation and scale are the same as in Fig. 4.

including both the brightest and faintest filaments. These comparisons make it clear that, although there are minor variations, the proper motion measurements should not depend critically on exactly which filaments are selected for measurement.

We have selected 18 positions for crosscuts to measure the average filament proper motion between the two epochs of *HST* data. In Figure 9, we show representative examples of these crosscuts in which a star in close proximity to relatively crisp, edge-on filaments has been used as a fiducial. The plots in the figure demonstrate again the relative uniformity of the offsets, and highlight how each crosscut can permit multiple measurements of the proper motion (from measurement of separate tangencies). From the measurement of 18 crosscuts across the WF2 and WF3 chips in field 1, using 14 different reference stars, we determine a proper motion of $0\farcs28 \pm 0\farcs03$ over the 1459 day ($\sim$4 yr) time interval between the images, or $0\farcs070 \pm 0\farcs008$ yr^{-1}. The corresponding number from the measurement in Paper I is $0\farcs081 \pm 0\farcs011$ yr^{-1}. These numbers are consistent within the errors, and hence no deceleration of the filament can be claimed. We note, however, that a modest deceleration of the filament by $\sim$20% over the last $\sim$50 yr is not precluded by the measurement. We use the two-epoch *HST* number, assuming no deceleration for the proper motion in the discussion below. By assuming no deceleration, our derived distance effectively becomes an upper limit on the true distance.

3.1.2. *Shock Velocity Estimate*

Our shock velocity estimate is weighted heavily by far-ultraviolet (FUV) spectroscopic observations of the field 1 filament, including significant results that have appeared since Paper I. Sankrit et al. (2000) have analyzed a STIS FUV/MAMA spectrum that was taken cutting across this filament. These data allowed an unprecedented measurement of the spatial distribution of FUV line emission in N v $\lambda\lambda$ 1239,1243, C iv $\lambda\lambda$1548,1550, and other lines behind the shock front. This analysis favored a shock velocity in the 170–180 km s^{-1} range, and preshock densities of 2–4 cm^{-3}. Also, lower spatial resolution Far Ultraviolet Spectroscopic Explorer (*FUSE*) observations of O vi $\lambda\lambda$1032,1038 as a function of position behind the shock (Sankrit & Blair 2002) have helped assess the postshock flow and geometry of the filament.

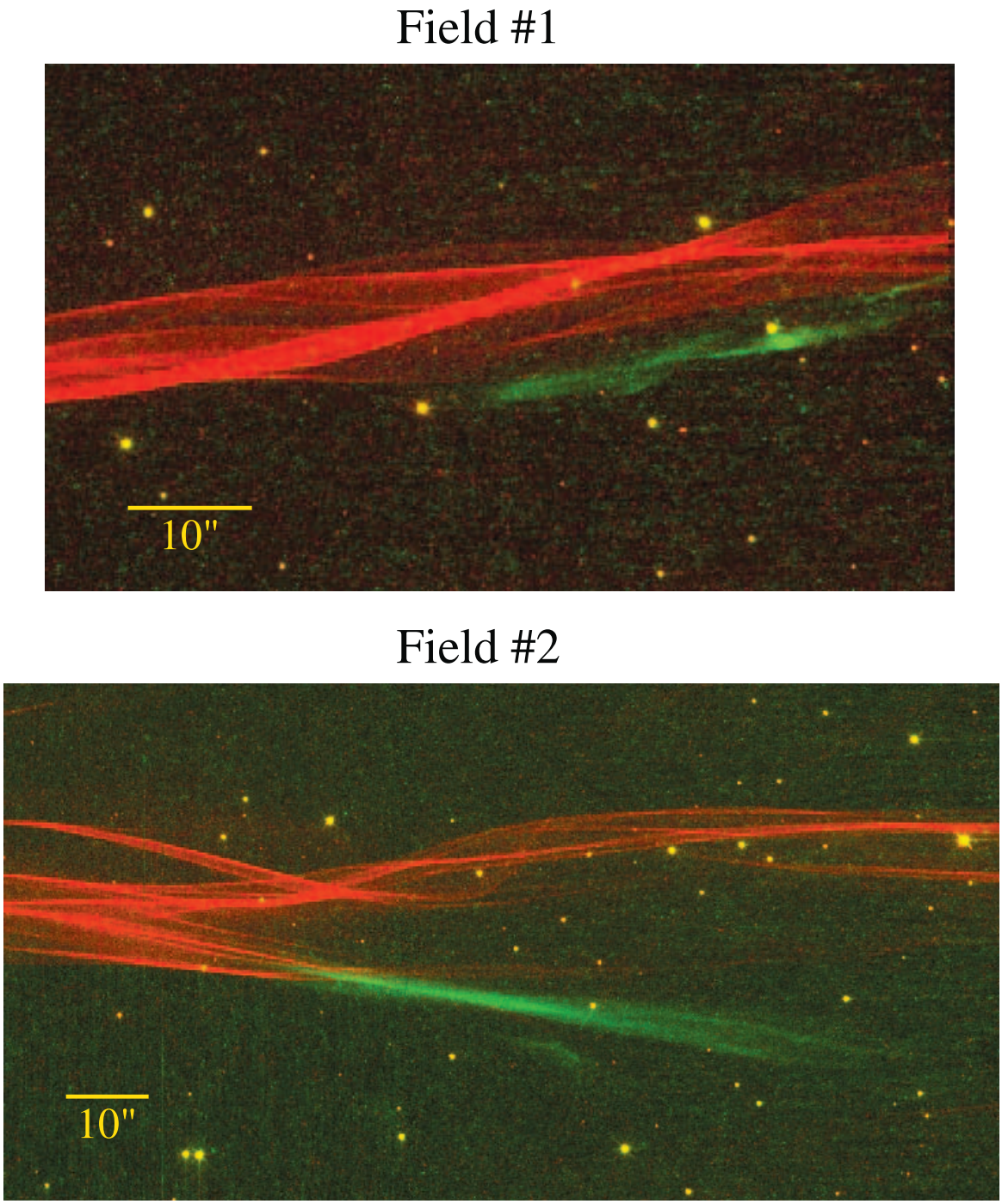

FIG. 6.—Enlargements of a portion of field 1 (*top*) and field 2 (*bottom*) showing the primary Hα–[O III] transition filaments. Note the "fuzzy" appearance of the [O III] regions and the relatively bright knot of [O III] emission in the top panel.

These results were also consistent with a shock velocity near 180 km s^{-1} within a fairly small range.

The Balmer line profiles of nonradiative shocks can also inform the shock velocity situation. The Balmer line emission comes from neutral atoms that pass through the shock front and are collisionally excited by electrons before becoming ionized (Chevalier & Raymond 1978). In this zone immediately behind the shock front, a significant fraction of the neutral hydrogen atoms undergo charge exchange with the hot postshock ions. This results in the Balmer lines having two distinct components—a narrow component with a thermal width representative of the preshock temperature and a broad component with a velocity spread representative of the postshock ion temperature. Since the postshock ion temperature depends on the shock velocity, the width of the broad component of the Hα line is a diagnostic for the shock velocity.

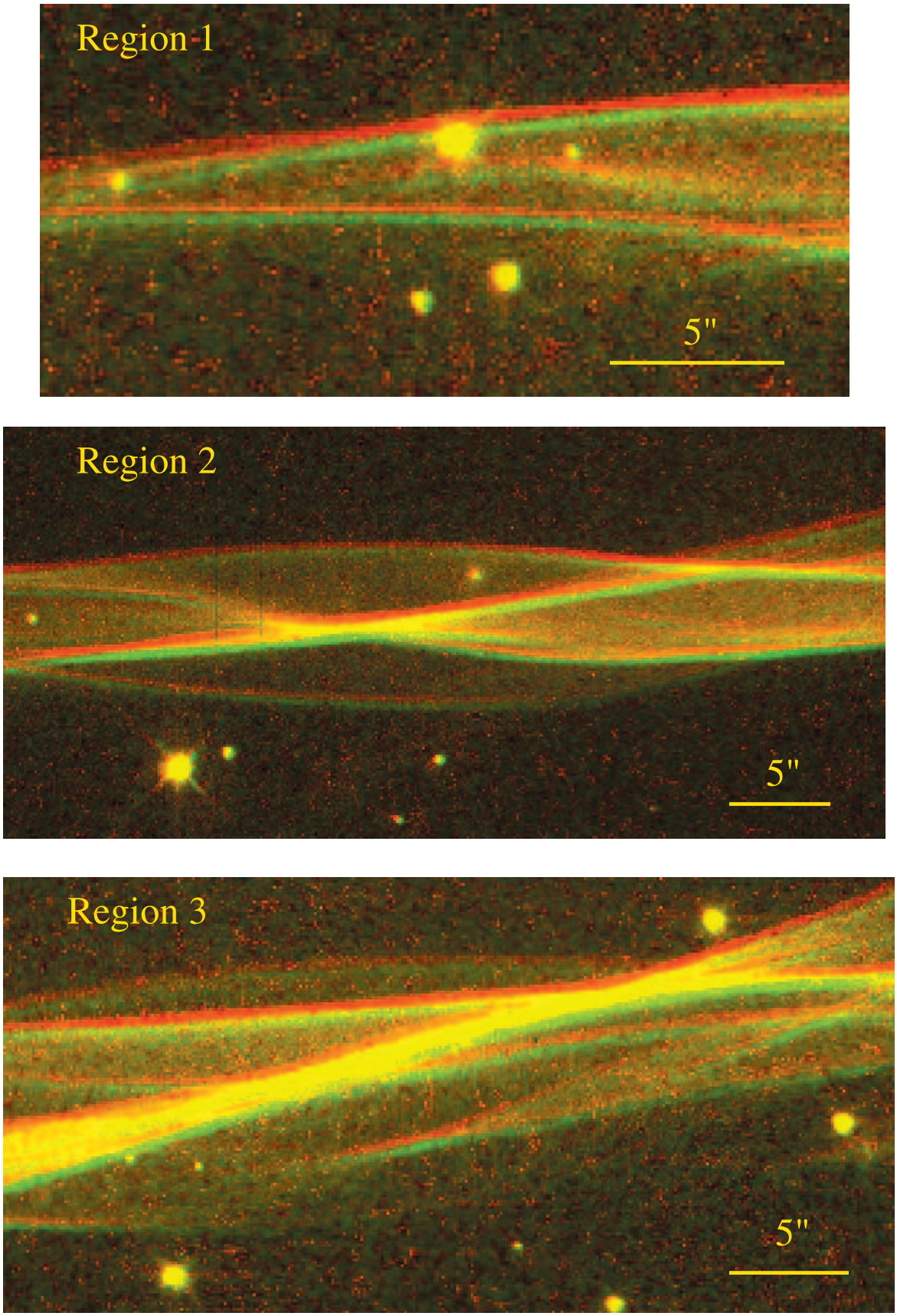

FIG. 7.—Three sections of field 1 enlarged to show the motions of the filament over a 4 yr period (boxes in Fig. 2 show the regions enlarged here). The yellow scale bar in each panel represents 5″. The red image is from 2001 and the green image is from 1997. Regions where emission is bright in both images appear yellow. These images show that the filament motion has been uniform and that no dramatic brightness changes have occurred over the 4 yr interval sampled.

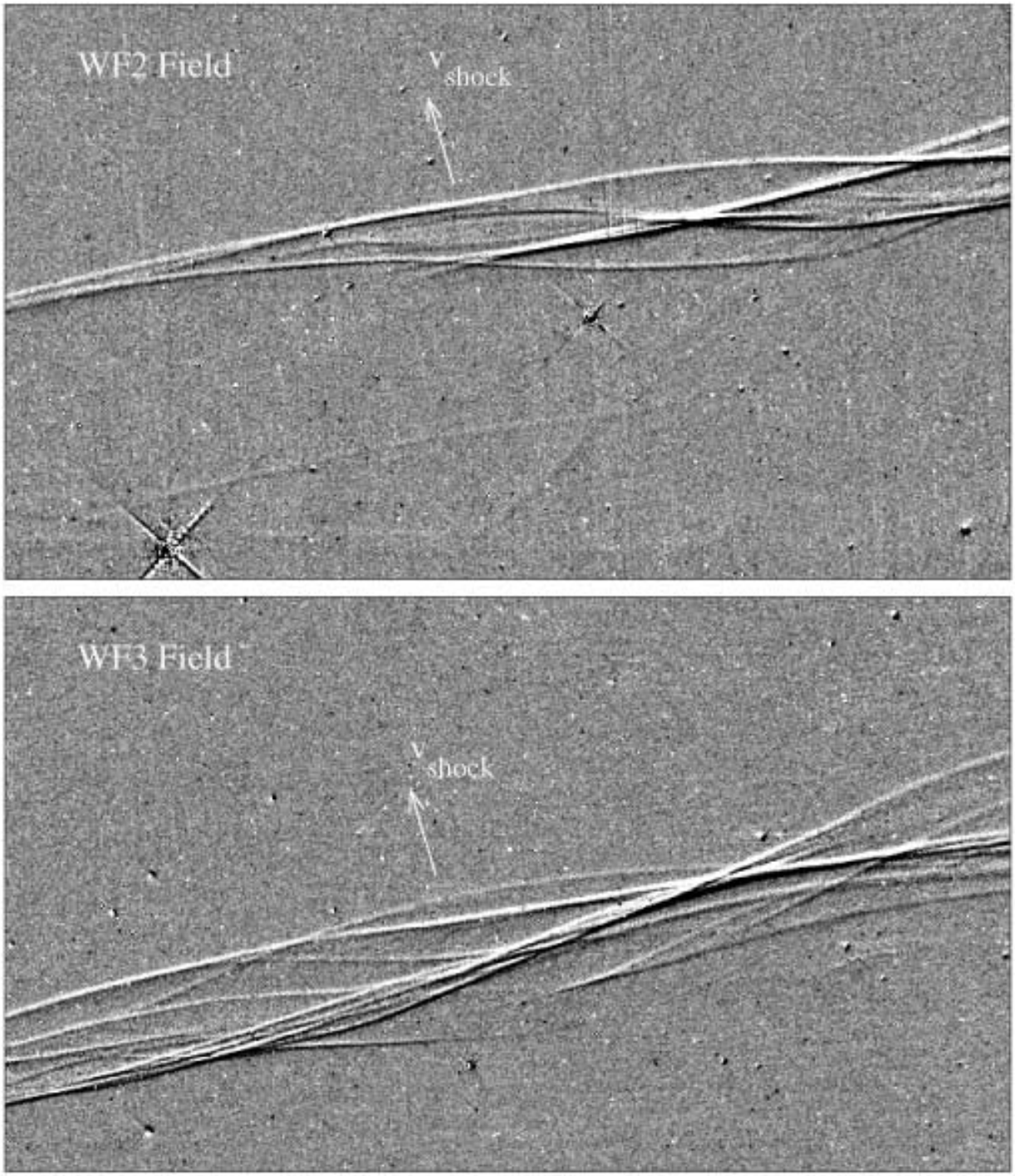

FIG. 8.—Difference images showing the field 1 filament motions over a 4 yr period. Separate regions from the WF2 and WF3 are shown. This version highlights how the filament motions visible in Fig. 7 extend throughout the filament structure, including the brighter and fainter filaments. Even some extremely faint filaments toward the bottom of each panel show up with this difference method. [*See the electronic edition of the Journal for a color version of this figure*.]

In detail, however, the conversion of an observed line width into a shock velocity depends on the way electrons and ions come into equilibrium in the postshock gas (e.g., Chevalier et al. 1980; Long et al. 1992; HRB94). Since Paper I, Ghavamian et al. (2001) have published a detailed observational and theoretical study of nonradiative shocks over a range of shock velocities, from Tycho's SNR ($V_{\rm br} = 1800$ km s^{-1}), to RCW 86 ($V_{\rm br} = 560$ km s^{-1}), to a Cygnus Loop nonradiative shock farther northwest along the same network of filaments observed in this paper ($V_{\rm br} = 350$ km s^{-1}; see Raymond et al. 2003). By observing and modeling the broad-to-narrow component ratios in both Hα and Hβ over a range of shock velocities, Ghavamian et al. (2001) found a correlation whereby the slower shocks are more equilibrated than the faster shocks. The observed broad-component width in the field 1 filament is between 130 and 167 km s^{-1} (Raymond et al. 1983; HRB94). As discussed in Paper I, there are reasons to suspect that the lower number was impacted somewhat by the slit geometry on the filament, and we estimate that a range of 150–167 km s^{-1} is more appropriate. Adopting this range, and equilibration in the 80%–100% range

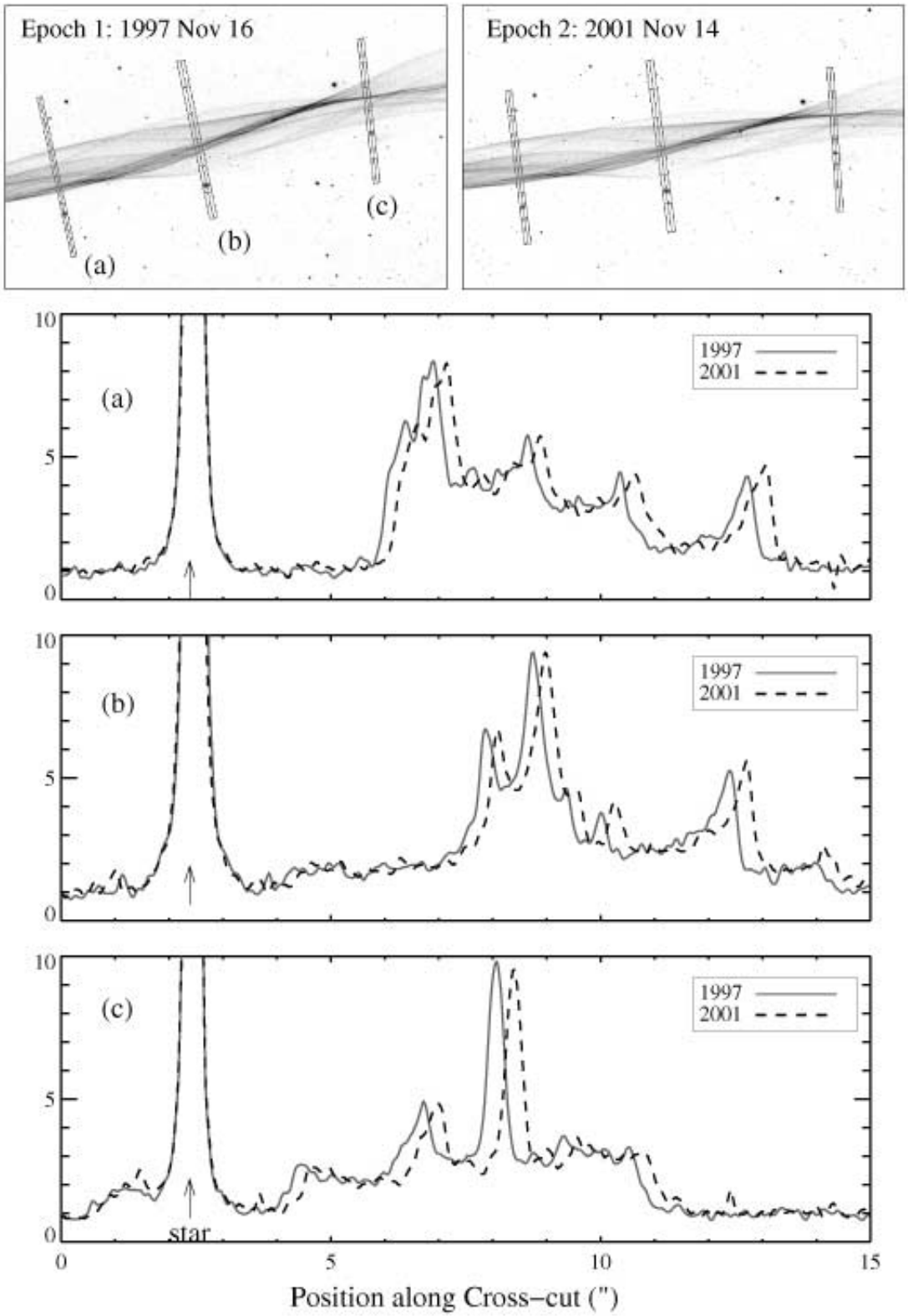

FIG. 9.—*Top two panels*: Three representative crosscuts in projection on the Hα images from 1997 and 2001. Each cut uses a star as a fiducial reference and traverses the local shock fronts as close to perpendicular as possible. *Lower panels*: Proper motion of the filaments over the 4 yr period. Epoch 1 data are shown as solid lines, and epoch 2 data are shown by dashed lines.

(cf. Ghavamian et al. 2001), a shock velocity of $V_{sh} = 182$–205 km s^{-1} is indicated.

The "highly equilibrated" assumption and recent FUV spectroscopic work are thus both consistent with a shock velocity somewhat higher than the 170 ± 20 km s^{-1} assumed in Paper I. Here we adopt a revised value of $V_{sh} = 180 \pm 10$ km s^{-1} as the best current estimate for the shock velocity of the field 1 filament.

3.1.3. *Revised Distance to the Cygnus Loop*

As in Paper I, we assume that the motion of the filament is perpendicular to our line of sight to derive the distance. For our best estimate values of $V_{sh} = 180 \pm 10$ km s^{-1} and proper motion $0''.070 \pm 0''.008$ yr^{-1}, we find a revised distance of $d \simeq 540^{+100}_{-80}$ pc for the Cygnus Loop, somewhat higher than the value found in Paper I but consistent within measurement errors.

In an upcoming paper (W. P. Blair et al. 2005, in preparation), we report an independent upper limit on the distance to the Cygnus Loop by constraining the distance to a star that is shown to be behind the Cygnus Loop. This measurement will further restrict the upper error bar on the measurement shown here.

3.2. *Comparison of* Hα *and* [O III] *Morphologies*

The basic morphological description of the filaments in the observed regions is that they represent thin sheets of emission seen almost exactly edge-on. Because the Hα emission arises in a very narrow region behind the shock front, the Hα images effectively represent snapshots of the shock front, with line-of-sight tangencies responsible for the sharpest (and typically brightest) filaments and slight nontangencies causing fainter, more diffuse emission regions that are adjacent. The faintest of these nontangent regions actually drops below detectability in Hα, but can be detected via their emission in stronger lines, such as O VI λ1032 (see Sankrit & Blair 2002). In addition, of course, we see complicated projection effects from ripples in the sheet along the line of sight, causing multiple, overlapping tangencies.

The general appearance of the [O III] emission is quite different from that of Hα. The [O III] filaments appear diffuse, although their position and shape compared with the Hα images (see Fig. 6) makes it likely that the [O III] filaments are simply extensions of filaments seen in Hα. One expects the [O III] region to be offset back from the Hα (downstream from the current shock position; e.g., Raymond et al. 1983), consistent with the appearance in the aligned images.

The fact that the observed [O III] filaments are not themselves bounded by Hα emission provides an important piece of information. Recall that the faint Hα emission seen in nonradiative shocks arises from neutral hydrogen in the preshock region that flows into the postshock region and undergoes excitation and recombination before becoming ionized. The preshock medium may be partially ionized, but some neutral hydrogen must be present to generate the Balmer line emission. Thus, the likely interpretation of the missing Balmer emission directly adjacent to the [O III] emission is that there is an additional ionizing flux generated in the nascent radiative filament that completely preionizes the preshock gas in the regions directly adjacent to the [O III]-emitting filaments. This appears to be a very local phenomenon, as opposed to the large-scale ionization structure reported by Bohigas et al. (1999).

3.3. *Implications of Filament Curvature*

The curvature in the shock fronts as seen in Figures 2 and 4 could in principle result from instabilities in the shock itself, or could reflect inhomogeneities in the preshock interstellar medium (ISM), since $V_s \propto n_0^{-1/2}$ for constant interior pressure. Raymond (2003) considered the ripples in a section of the nonradiative shock farther to the northwest, the filament called P7 observed with the Hopkins Ultraviolet Telescope (HUT) and *FUSE* (Raymond et al. 2003). That filament has a higher shock speed and lower pre-shock density, so that radiative cooling is insignificant and neither thermal instability (e.g., Gaetz et al. 1988; Innes 1992) nor the thin shell instability (Vishniac 1983; Vishniac & Ryu 1989) can operate. The Hα image of that filament showed ripples with an amplitude about 10% of their $\sim$0.8 pc wavelengths. Because they cannot be attributed to shock instabilities, Raymond (2003) interpreted the ripples as 10% variations in shock speed caused by 20% variations in pre-shock density, plausibly associated with the overall turbulence of the ISM inferred from radio scintillation studies (Lovell et al. 2003 and references therein).

The ripples in Figures 2 and 4 also show amplitudes of order 10% of their wavelengths, but the wavelengths are about 3 times smaller than for the P7 region discussed above. In this case, radiative cooling is important, as shown by the presence of some [O III] (Figs. 3 and 5) and by ultraviolet spectra (Raymond et al. 1983; Long et al. 1992). Since the cooling is just beginning, the thin shell instability would not have had time to develop, but thermal instabilities might be starting to occur. On the basis of the Gaetz et al. (1988) model of a 200 km s^{-1} shock, the amplitude of the ripples should be comparable to the cooling length behind the shock. Inspection of Figure 6 suggests that this may be the case.

Preshock density fluctuations might also be the cause of, or at least an important contributing factor to, the observed structures. The density fluctuations for a Kolmogorov spectrum would be expected to be $3^{5/3} \simeq 6$ times smaller at this scale than at the scale inferred for filament P7, so the ripple amplitude would be only about 2.5% of the wavelength. However, it is simplistic to try to separate thermal instabilities from the preshock density fluctuations for a shock in transition from the nonradiative to the radiative phase. Some perturbation is needed to produce a significant amplitude thermal instability during the first cooling time, and the instability will greatly amplify whatever perturbation exists. The cooling distance for shocks in this velocity range scales roughly as

$$l \propto vt_c \propto v\frac{T}{n\Lambda} \propto v^6, \tag{1}$$

where the cooling time t_c is given by the temperature T, which scales as v^2, divided by the cooling coefficient Λ, which is proportional to $T^{-1/2}$ for 10^5–10^7 K, and the density, which is proportional to v^{-2} if the ram pressure is constant (Raymond et al. 1976). Thus, a 2% shock velocity fluctuation can be amplified to a 12% variation in cooling length quite easily.

The Hα observation in field 2 (Fig. 4) provides some surprising examples of Balmer filaments with a much larger curvature projected onto the plane of the sky than has been seen previously. In Figure 10, we show an enlarged portion of the field 2 Hα image in which a circular Gaussian filter has been applied ($\sigma = 4$ pixels). While this decreases the resolution overall, it tends to decrease the pixelation in the background, making it somewhat easier to trace these faint filamentary structures against the background. The filament labeled "filament 1" in Figure 10 provides the primary example, where the rippled filament can be followed toward the lower left until it merges smoothly with one of the tangencies in the brighter filament region. A second filament, labeled "filament 2," is somewhat fainter but appears to closely parallel filament 1, apparently

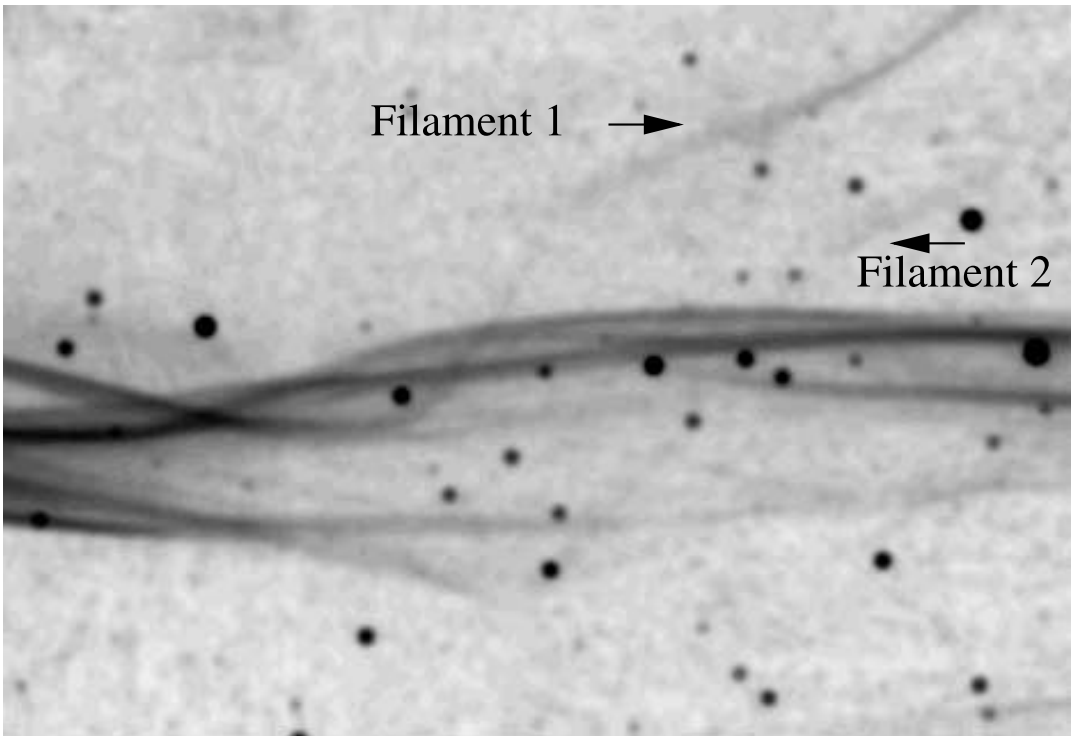

FIG. 10.—Portion of the field 2 Hα image showing the filaments with strong curvature, after smoothing with a circular Gaussian filter with $\sigma = 4$ pixels to reduce the pixelation in the background noise. Two filaments, labeled filament 1 and filament 2, are discussed in the text.

delineating a second tangency of the same shock front structure. The connection of filament 2 back into the main filament structure is less clear, owing both to the faintness of this filament and the fact that the connection region is in an area of complex projection effects (including the Hα to [O III] transition filament discussed earlier; see Fig. 6).

Moving from left to right in Figure 10, filament 1 undergoes a change in angle of some 60° over just a few arcseconds of filament length, traverses nearly radially for some 10″–12″, and then bends back by some 40° before exiting the figure at the upper right. In spite of the sharp bends, the separation between this filament and the others is only about twice the separation of the other filaments from each other at the right edge of Figure 10. The surface brightness of the filaments in the middle region of filament 1 is somewhat lower than adjacent sections, but this could be due to geometry or changing neutral preshock fraction. Assuming that the brighter Hα filaments have been propagating through their present physical conditions for a cooling time of roughly $4900/n_0$ yr at $V_s = 200$ km s^{-1} (Hartigan et al. 1987), and assuming a preshock density of 1–2 cm^{-3} (Long et al. 1992; HRB94), the faster portion of the shock is only about 10% faster than the slower portion. Thus, while the sharp bend requires a fairly steep density gradient, the actual density contrast may be as little as 20%. Hence, it does not require a dramatic change of preshock conditions to account for the observed filament morphology.

4. SUMMARY

HST WFPC2 imagery in the northeastern Cygnus Loop has been used to study the motion, structure, and dynamical state of the primary Cygnus Loop blast wave as it encounters the surrounding medium. Although the shocks are primarily nonradiative, there are isolated sections of these shocks that are becoming radiative, as indicated by [O III] λ5007 emission. The smooth morphology and undulating appearance of the shock tangencies limit the presence of small-scale instabilities. The observed rippling can be explained by very modest local changes in shock velocity and/or preshock density.

Our imagery provides second-epoch Hα coverage of one field. We use these data to study the motion of the filament structure over 4 yr. Only minor variations from a mean proper motion are detectable in this 4 yr baseline, and we find little change in the relative surface brightnesses of the observed filaments. The proper motion found here is modestly smaller than that found in Paper I but is consistent within errors. The new proper motion and best estimate of the shock velocity in this region are used to calculate a revised distance of 540^{+100}_{-80} pc to the Cygnus Loop, assuming no deceleration of the filament.

This work has been supported by STScI grant GO-09080.01A to Johns Hopkins University.

REFERENCES

Blair, W. P., Sankrit, R., Raymond, J. C., & Long, K. S. 1999, AJ, 118, 942
Bohigas, J., Sauvageot, J. L., & Decourchelle, A. 1999, ApJ, 518, 324
Chevalier, R. A., Kirshner, R. P., & Raymond, J. C. 1980, ApJ, 235, 186
Chevalier, R. A., & Raymond, J. C. 1978, ApJ, 225, L27
Gaetz, T. J., Edgar, R. J., & Chevalier, R. A. 1988, ApJ, 329, 927
Ghavamian, P., Raymond, J. C., Smith, R. C., & Hartigan, P. 2001, ApJ, 547, 995
Hartigan, P., Raymond, J., & Hartmann, L. 1987, ApJ, 316, 323
Hester, J. J., Raymond, J. C., & Blair, W. P. 1994, ApJ, 420, 721 (HRB94)
Innes, D. E. 1992, A&A, 256, 660
Leahy, D. A. 2002, AJ, 123, 2689
———. 2003, ApJ, 586, 224
———. 2004, MNRAS, 351, 385
Levenson, N. A., et al. 1997, ApJ, 484, 304

Long, K. S., Blair, W. P., Vancura, O., Bowers, C. W., Davidsen, A. F., & Raymond, J. C. 1992, ApJ, 400, 214
Lovell, J. E. J., Jauncey, D. L., Bignall, H. E., Kedziora-Chudczer, L., Macquart, J.-P., Rickett, B. J., & Tzioumis, A. K. 2003, AJ, 126, 1699
Minkowski, R. 1958, Rev. Mod. Phys., 30, 1048
Raymond, J. C. 2003, Rev. Mexicana Astron. Astrofis., 15, 258
Raymond, J. C., Blair, W. P., Fesen, R. A., & Gull, T. R. 1983, ApJ, 275, 636
Raymond, J. C., Cox, D. P., & Smith, B. W. 1976, ApJ, 204, 290
Raymond, J. C., Ghavamian, P., Sankrit, R., Blair, W. P., & Curiel, S. 2003, ApJ, 584, 770
Sankrit, R., & Blair, W. P. 2002, ApJ, 565, 297
Sankrit, R., Blair, W. P., Raymond, J. C., & Long, K. S. 2000, AJ, 120, 1925
Vishniac, E. T. 1983, ApJ, 274, 152
Vishniac, E. T., & Ryu, D. 1989, ApJ, 337, 917